Si/SiGe Bound-to-continuum Terahertz Quantum Cascade Emitters

D.J. Paul[a], G. Matmon[b], L. Lever[c], Z. Ikonic[c], R.W. Kelsall[c] D. Chrastina[d], G. Isella[d], H. von Känel[d], E. Müller[e] and A. Neels[f]

[a] Department of Electronics and Electrical Engineering, University of Glasgow, Glasgow, G12 8LT, U.K.
[b] Cavendish Laboratory, University of Cambridge, Cambridge, CB3 0HE, U.K.
[c] Department of Electronic and Electrical Engineering, University of Leeds, Leeds, LS2 9JT, U.K.
[d] CNISM and L-NESS, Politecnico de Milano, I-22100 Como, Italy
[e] Electron Microscopy ETH Zürich, ETH Zürich, CH-8093 Zürich, Switzerland
[f] Institute of Microtechnology, University of Neuchâtel, CH-2002 Neuchâtel, Switzerland

Si/SiGe bound-to-continuum quantum cascade emitters designed by self-consistent 6-band **k.p** modeling and grown by low energy plasma enhanced chemical vapour deposition are presented demonstrating electroluminescence between 1.5 and 3 THz. The electroluminescence is Stark shifted by an electric field and demonstrates polarized emission consistent with the design. Transmission electron microscopy and x-ray diffraction are also presented to characterize the thick heterolayer structure.

Introduction

The terahertz (THz) part of the electromagnetic spectrum has a number of potential applications which include oncology (skin cancer imaging (1)), security imaging (2), production monitoring, polution monitoring and astronomy. The key to the take up of THz in many of these potential markets is the ability to produce cheap, fast, high-performance imaging systems which requires high power sources, cheap passive optics and large focal plane imaging arrays of detectors. GaAs quantum cascade lasers (QCLs (3)) have demonstrated high power outputs at THz frequencies, up to 248 mW at 4 K operating temperature (4), but this output power is significantly reduced as the operating temperature is increased. The highest operating temperature demonstrated is 178 K but at the cost of the output power being reduced to ~ 1 mW (5).

The reduction in output power is partly related to the polar optical phonon scattering in III-V materials which results in the non-radiative lifetimes of the subband states being reduced significantly as the temperature increases (6). The lack of polar optical phonon scattering in Group IV materials produces a far weaker decrease in the lifetime as the temperature increases (7)(8)(9). Experiments with $Si_{0.4}Ge_{0.6}$ quantum wells have demonstrated subband lifetime reductions of only a factor of 2 between 4 K and 225 K (9). Therefore the lack of polar optical phonon scattering coupled with lower free carrier absorption and the higher thermal conductivity of the Si substrate could allow significantly higher operating temperatures for Si/SiGe THz QCLs. The lack of polar optical phonon scattering, however, paradoxically also makes population inversion more difficult to engineer as resonant depopulation of a lower radiative subband cannot be achieved using optical phonons in Group IV materials. Si based devices would also benefit from the mature Si process technology resulting in lower manufacturing costs.

There have been a number of demonstrations of electroluminescence from Si/SiGe quantum cascade designs both at mid-infrared (10)(11) and THz frequencies (12)(13). Due to the large electron effective mass in the tunnel direction for Si (100) substrates and the surface segregation of n-type dopants in gas source Si/SiGe deposition systems, all Si/SiGe quantum cascade structures demonstrated to date have been designed to use holes rather than electrons. At THz, both intrawell (12) and interwell (13) staircase structures have demonstrated strong electroluminescence but suffer from poor injection efficiency limiting the gain from the designs. The lowest reported Si/SiGe waveguide losses at appropriate THz frequencies requires at least 16 cm^{-1} of gain (14) from a quantum cascade design to achieve lasing and this has yet to be achieved.

One of the most successful designs for III-V QCLs is the bound-to-continuum structure (15) where a single bound subband state is used for the upper radiative subband. A miniband is used as the lower radiative subband states with intraminiband scattering providing fast extraction of electrons allowing population inversion to be engineered. The miniband also provides efficient injection into the next cascade period bound subband state. While the bound-to-continuum design has been demonstrated before in Si/SiGe heterostructures at mid-infrared frequencies (11), no electroluminescence was observed at THz frequencies (16), believed to be due to scattering of carriers to parasitic light-hole (LH) states. In this paper, clear THz electroluminescence is achieved by straining the parasitic LH states to be far higher in hole energy than the heavy-hole (HH) subband states used for the transition and the miniband.

Design, Deposition and Physical Characterisation of Cascade Structure

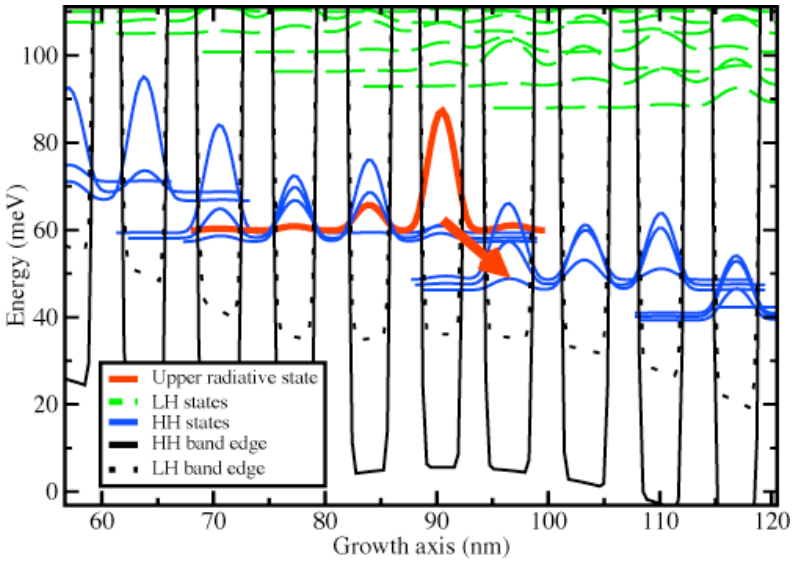

Figure 1. The squared envelope functions of the HH (solid lines) and LH (dashed lines) in one period of the quantum cascade design at 4 kV/cm. The heterolayer compositions and thicknesses are described in the main text.

A self-consistent 6-band **k.p** modeling tool (8)(9) was used to design the HH to HH bound-to-continuum hole quantum cascade structure shown in Figure 1. The valence band diagram is shown at an applied electric field across the device of 4 kV/cm and clear band-bending is observed in each period due to the redistribution of charge. Hole energy is plotted up the page so holes flow from top left to bottom right in the figure. The squared envelope functions of HH subbands are shown in solid lines and LH states are

dashed. The arrow indicates the radiative transition between the upper radiative HH bound state to the lower HH miniband. Strain engineering was used to shift the LH states to higher energy than the active HH states thus reducing the non-radiative depopulation of the upper HH level.

The wafers were grown by low energy plasma enhanced chemical vapour deposition (LEPECVD) (17) which has the advantage of high growth rates making the technique ideal for the thick heterostructures required for QCLs as well as microelectronic (18) and optoelectronic (19)(20) Si/SiGe devices. SiH_4 and GeH_4 precursor gases were used along with B_2H_6 for doping. A linearly graded $Si_{1-y}Ge_y$ buffer was grown graded at 7%/μm Ge content and capped with a 2 μm constant composition $Si_{0.65}Ge_{0.35}$ buffer, all grown at ~10 nm/s. A 500 nm p-$Si_{0.65}Ge_{0.35}$ contact layer was followed by a 44 nm $Si_{1-x}Ge_x$ injector graded from x=0.34 to x=0.44 and doped at 10^{17} cm^{-3}. 100 periods of the active cascade design was then grown at 550 ˚C at 13 nm/min consisting of (bold text indicates Si barriers, normal text indicates $Si_{0.5}Ge_{0.5}$ quantum wells): **1.75**, 3.61, **0.94**, 4.81, **1.48**, 4.51, **p-1.61**, 4.21, **p-1.75**, 4.21, **1.88**, 3.91, **2.02**, 3.91. While two significant figures are used for these heterolayer thicknesses, each heterolayer is chosen to be an integer number of monolayers. Two of the barriers were doped to provide a sheet density of $5x10^{11}$ cm^{-2} as indicated. The final extractor and contact layers consisted of 1.75 nm Si, 3.75 nm $Si_{0.5}Ge_{0.5}$, 0.94 nm Si, 86 nm graded $Si_{1-x}Ge_x$ (x=0.44 to x=0.34) doped at 10^{17} cm^{-3}, 50 nm p-$Si_{0.65}Ge_{0.35}$ and a 5 nm p-Si cap both doped at 10^{19} cm^{-3}.

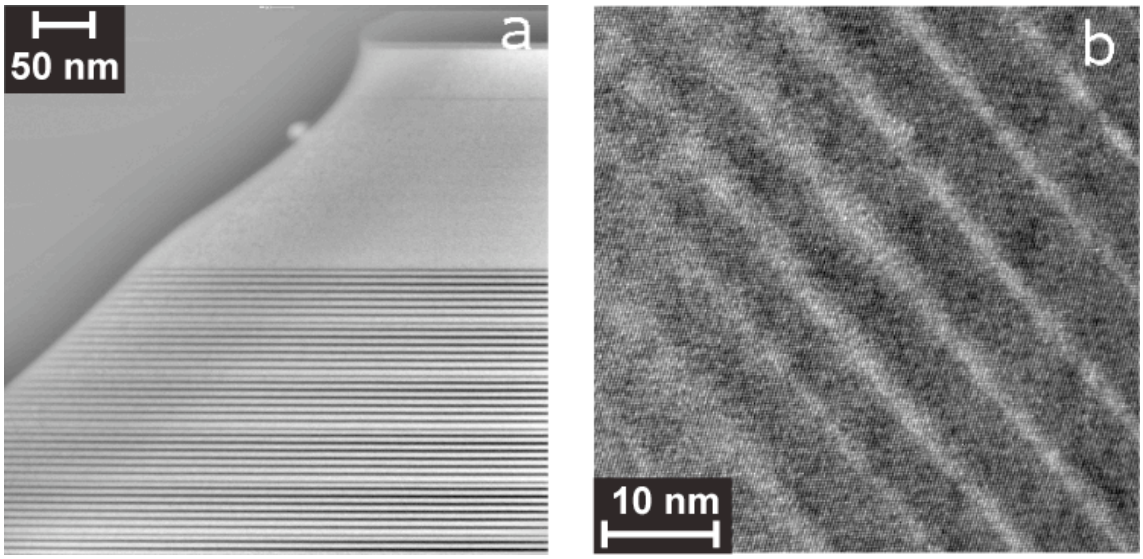

Figure 2. TEM images of the deposited quantum cascade heterolayers. a) shows a high pass filtered high angle annular dark field scanning TEM image of the surface heterolayers of the wafer with 4 periods of the quantum cascade design along with the extractor and contact capping layers and b) shows a high resolution image of one period of the quantum cascade deposited structure.

Both transmission electron microscopy (TEM) and X-ray diffraction has been used to characterize the heterolayers in the deposited wafer. Samples were taken from the centre of the wafer. Figure 2 shows TEM images of the quantum cascade stack taken using a Philips CM30 microscope. The lower resolution image on the left shows the capping layers of the wafer and the top 4 cascade periods with the extractor and contact layers. A high resolution image is shown on the right of one period of the cascade. The

TEM images demonstrate a high level of planarity of the heterolayers and good growth uniformity between the first and last cascade periods (less that 2% variation in thickness).

High resolution x-ray diffraction (HRXRD) was performed with ω-2θ scans and reciprocal space mapping in the vicinity of the (004) and (115) reflections. A scan through the (004) reflection is shown in Figure 3. Dynamical simulations were used to extract the structural parameters from the data. The Ge content in the virtual substrate obtained was found to be 34.6% which is extremely close to the design value of 35%. The relaxed buffer peak, however, is shifted from the 0^{th} order superlattice peak, indicating that the strain compensation in the structure is not perfect. There is also a small tilt of 0.30˚ between the relaxed buffer and the quantum cascade superlattice periods. The HRXRD dynamical simulations and the TEM images indicate that the quantum cascade period is 53 nm which is larger than the designed value of 40.6 nm. Also the simulations extract the Ge content in the quantum wells as 45% which is lower than the design value of 50%.

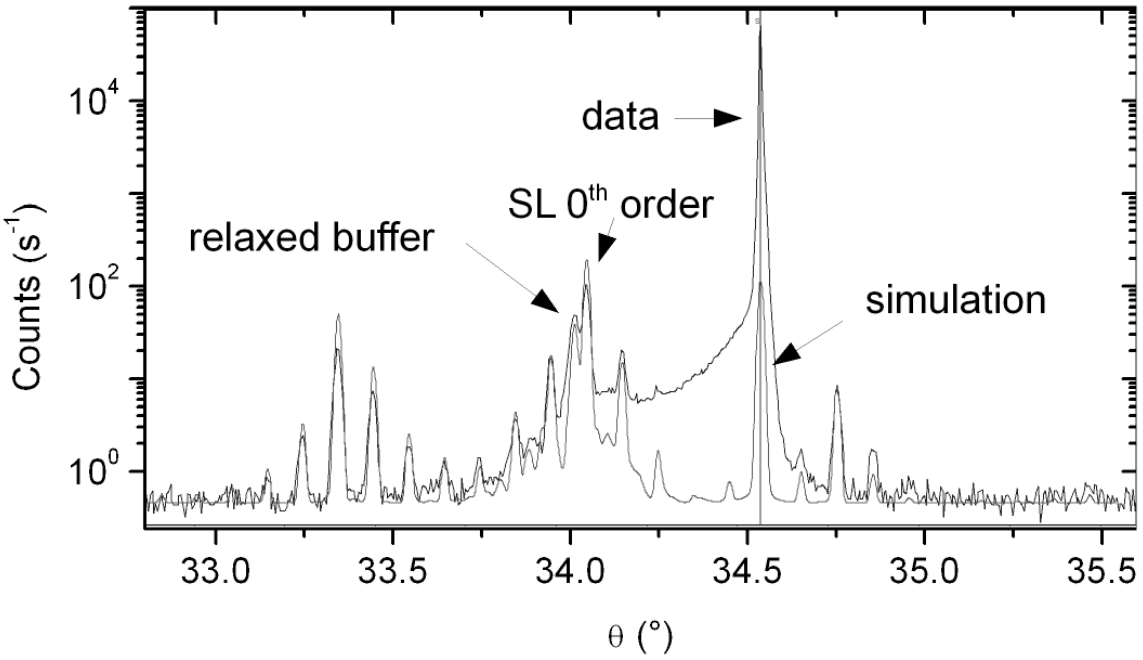

Figure 3. HRXRD ω-2θ scan through the (004) reflection of the quantum cascade heterostructure. The Ge content, strain state and superlattice period were extracted by using dynamical simulations.

While the uniformity of the growth rate over the 5 hour LEPECVD growth of the full 100 periods of the quantum cascade structure shows excellent uniformity, the present LEPECVD reactor has known non-uniformity across the diameter of a 100 mm wafer. The growth rate is known to decrease towards the edge of the wafer. While the TEM and HRXRD have produced a period thickness of 53 nm at the centre of the wafer, samples for electrical and optical characterization were taken from the edge of the wafer where the period should be smaller and hopefully closer to the design period length of 40.6 nm.

Electrical and Optical Characterisation

Samples for electrical and optical measurements were processed into 7 mm x 75 μm ridge waveguides using the Bosch process reactive ion etching. Lift-off was used to deposit Ni as the top contact on top of the ridge and Al (1% Si) as the bottom contact.

Both were then annealed at 450 ˚C to produce a shallow NiSi contact on top of the superlattice and a spiked Al bottom contact. Previous tests of both technologies has indicated that this arrangement provides the lowest contact resistivities and therefore the lowest heating to the device. The samples were back coated with Ti/Au before being indium bonded to Ti/Au coated copper mounts to ensure good thermal contact to the cold finger of the continuous flow cryostat.

Fourier transform infrared spectroscopy (FTIR) was performed using a Bruker 66vs FTIR in stepscan mode using a liquid He cooled QMC Si bolometer as detector (12). The cryostat with the device for test sits inside a purpose build emission box bolted to the FTIR system allowing all parts of the system inside which THz radiation propagates to be either under vacuum or purged with dry N_2 gas. A voltage was applied vertically across the top and bottom contacts to the device using a 10 kHz square wave pulse stream at varying duty cycles, gated by a 387 Hz 50% duty cycle square wave used for lockin purposes of the detector (13). Three separate samples were fabricated and tested showing nominally identical results. Due to space limitations, the results from one device will be presented below.

Figure 4 shows the luminescence-current-voltage (LIV) measurements of the device in the emission chamber with the mirrors on the arms of the Michelson interferometer positioned at equal distances. Below 3 kV/cm, the electroluminescence power is due to radiative transitions between the hydrogenic impurity states of the boron dopant (21)(22) either in the quantum cascade periods, the doped Ohmic contact layers to the quantum cascade structure or more likely from the p-type Si substrate. Above 3 kV/cm applied bias, the subband states start to align in the device and a near linear electroluminescent power dependence on current density is observed.

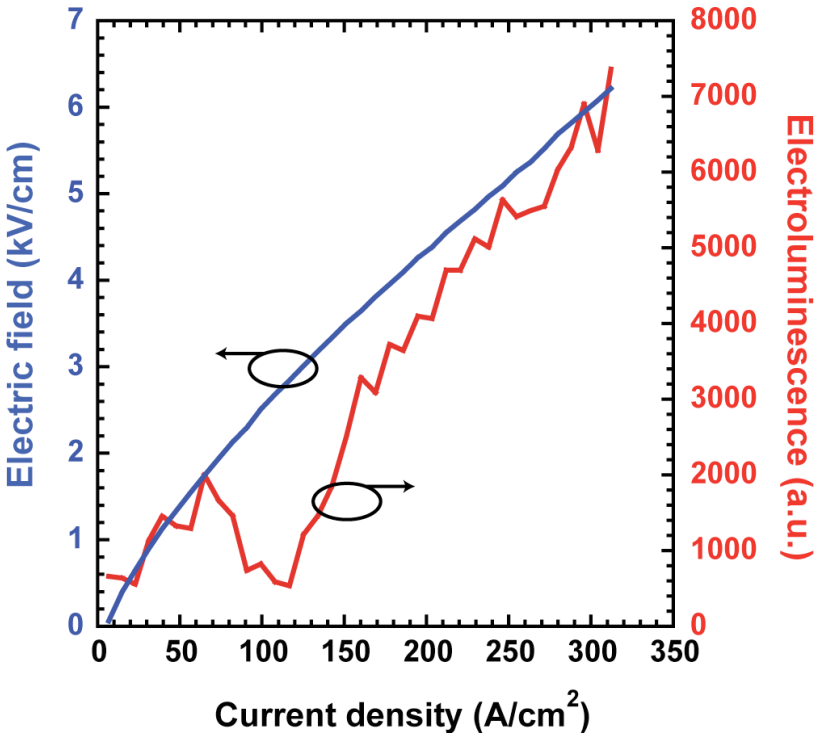

Figure 4. The electric field and the electroluminescence power as a function of the current density applied through one cascade device at 4.2 K with 10 % duty cycle.

The electroluminescence spectrum at 5 kV/cm is shown in Figure 5 compared to the predictions from the self-consistent 6-band **k.p** theory for a single radiative transition from the bound state to a single subband in the miniband. The experimental peak full width half maxima (FWHM) is around 10 meV, one of the smallest reported in SiGe hole devices. It is clear from the spectra that the electrolumescence peak is made up of a number of transitions from the upper states to the miniband. It is also likely that some of the peak width is due to heating but this is extremely difficult to measure and quantify using the present experimental setup.

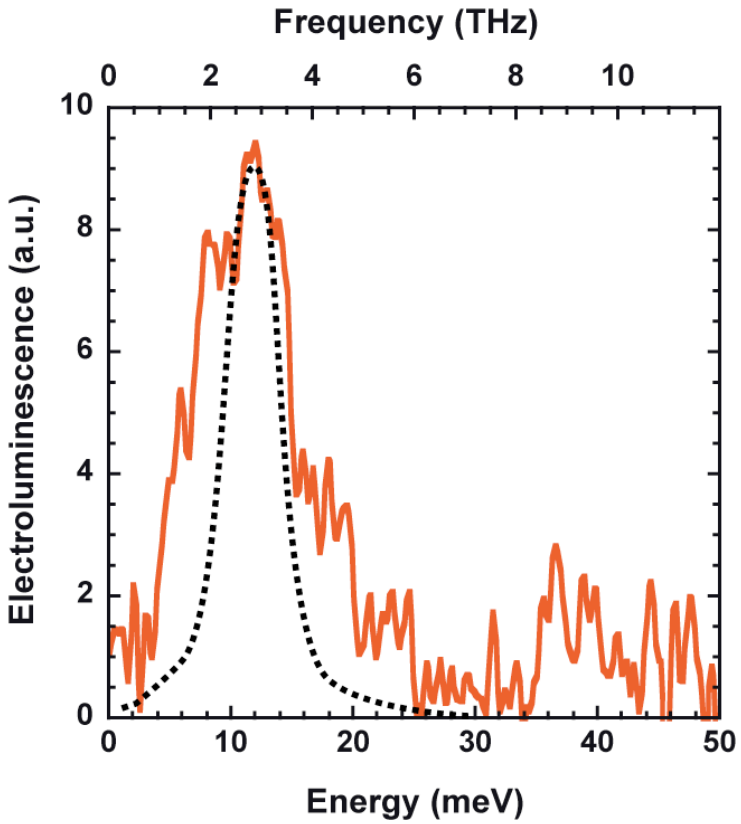

Figure 5. The solid line is the electroluminescence at 4.2 K and 5 kV/cm applied electric field with 10% duty cycle. The dashed line is calculated by self-consistent 6-band **k.p** theory for radiative transitions from the bound state to a single subband in the miniband.

As the electric field in the sample is changed, the alignment of the subband states and the pseudo-diagonal (interwell) radiative transition should change. This is shown experimentally in Figure 6 where the electroluminescence spectrum is shown for 3 different electric fields demonstrating a Stark shift of the peak. Modelling of the electroluminescence peak shift using the **k.p** tool (not shown in Figure 6 for clarity) demonstrates a peak shift comparable to the experimental results but does not show any significant increase in FWHM at the level demonstrated by the experimental results. While higher heating is expected at higher electric fields, the structure shown in the electroluminescence spectra suggests that some additional radiative subband transitions are becoming active at higher electric fields. The miniband in the bound-to-continuum design provides a range of subband states which can participate in radiative transitions and the large band bending (see Figure 1) in this structure due to the charge redistribution will also change as the electric field across the device is changed. The experimental results are therefore as should be expected for this design of quantum cascade period.

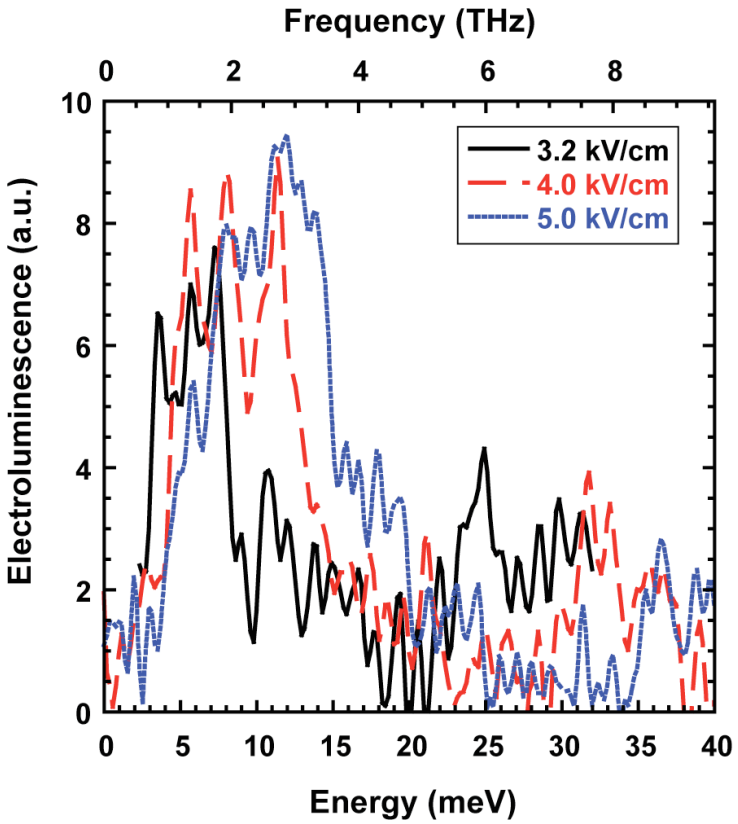

Figure 6. The electroluminescence spectrum plotted for three different applied electric fields at 10% duty cycle and 4.2 K. A Stark shift is observed as the electric field is increased.

In the parabolic approximation, a HH to HH transition at $k_{//} = 0$ should only have a TM polarized component with the TE component forbidden through selection rules. LH to HH transitions have both TM and TE polarized components (13). This selection rule is relaxed away from $k_{//} = 0$ where non-parabolicity and band mixing can result in a finite TE component. As the $k_{//}$ vector is increased, the mixing of the HH and LH bands increases and the TE component also increases. The insert to Figure 7 shows the dispersions of two of the subband states involved in the radiative transition i.e. the bound state and one of the subbands in the miniband. As $k_{//}$ increases (where there is more LH character from mixing and therefore more TE polarized component) the subbands are closer together resulting in lower energy transitions. Therefore the theory predicts that the TE polarized emission should be lower in energy to the TM polarized emission. This is observed in the experimental results shown in Figure 7 where the TM polarized peak is at a small but significantly higher energy than the TE polarized component.

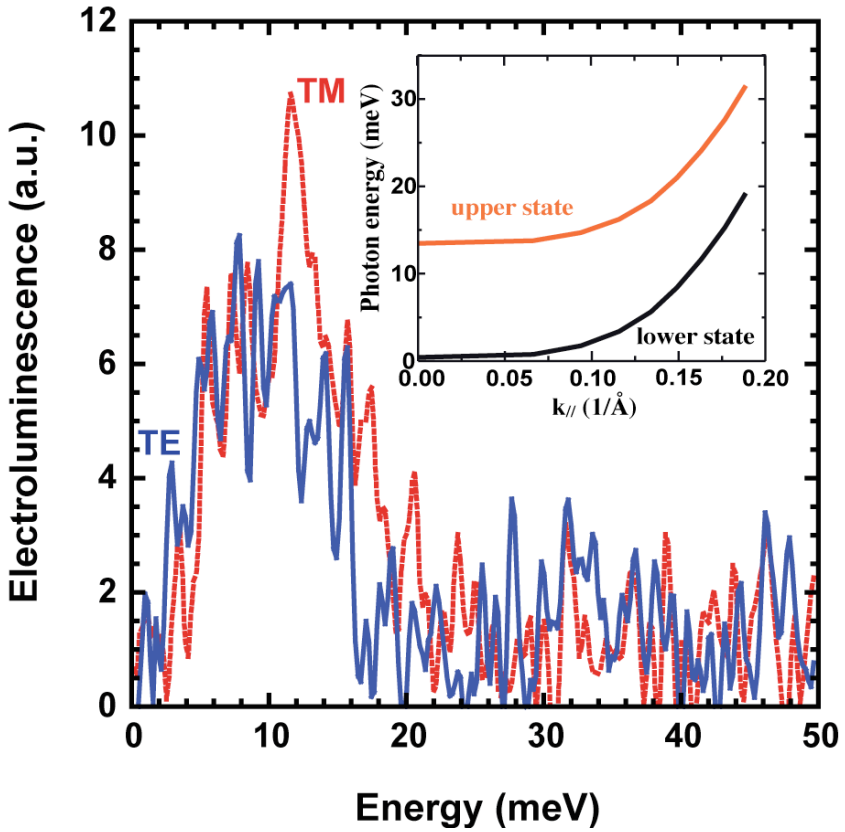

Figure 7. The TM (dashed line) and TE (solid line) polarized spectra for one cascade sample at 4.2 K, 10% duty cycle and 8 kV/cm. The insert shows the $k_{//}$ dispersion for the radiative subband states ($k_x = k_y$) showing a decrease in the transition energy as $k_{//}$ increases.

Conclusions

A HH to HH bound-to-continuum structure designed using a self-consistent 6-band **k.p** tool was investigated to investigate the potential of producing a Si/SiGe QCL at THz frequencies. Results were presented demonstrated intersubband electroluminescence from a 100 period Si/SiGe quantum cascade structure grown by LEPECVD. TEM and HRXRD have been used to characterize the cascade structure and have shown that the grown period at the centre of the wafer is greater than the designed structure. The structural characterization also demonstrates excellent growth uniformity through the total growth of the 100 period quantum cascade superlattice with the first and last periods differing by less than 2% in heterolayer thicknesses. Increase of the applied electric field results in the electroluminescence peak being Stark shifted to higher emission energies. While the structure is a HH to HH design, both TE and TM polarized emission spectra were obtained but the spectra agree with the predictions of theory. While the present design does not yet have enough gain to achieve lasing, the results demonstrate the robustness of the bound-to-continuum design to tolerate small heterolayer thickness variations in the growth of the structure.

Acknowledgments

The authors would like to thank the Cariplo Foundation through the SIMBAD project and the DTI Micro and Nanotechnology Initiative for finacial support.

References

1. P.H. Siegel, *IEEE Trans. Microwave Theory*, **52**, 2438 (2004).
2. A.G. Davies, A.D. Burnett, W.Fan, E.H. Linfield and J.E. Cunningham, *Materials Today.*, **11(3)**, 18 (2008).
3. R. Köhler, A. Tredicucci, F. Beltram, H.E. Beere, E.H. Linfield, A.G. Davies, D.A. Ritchie, R.C. Iotti and F. Rossi, *Nature*, **417**, 156 (2002).
4. B. S. Williams and S. Kumar and Q. Hu and J. L. Reno, *Elec. Lett.*, **42**, 89 (2006).
5. M.A. Belkin, J.A. Fan, S. Hormoz, F. Capasso, S.P. Khanna, M. Lachab, A.G. Davies and E.H. Linfield, *Opt. Exp.,* **16**, 3242 (2008).
6. B.N. Murdin, W. Heiss, C.J.G.M. Langerak, S.C. Lee, I. Galbraith, G. Strasser, E. Gornik, M. Helm and C.R. Pidgeon, *Phys. Rev. B* **55**, 5171 (1997).
7. P. Murzyn, C.R. Pidgeon, J.P.R. Wells, I.V. Bradley, Z. Ikonic, R.W. Kelsall, P. Harrison, S.A. Lynch, D.J. Paul, D.D. Arnone, D.J. Robbins, D.J. Norris and A.G. Cullis, *Appl. Phys. Lett.*, **80**, 1456 (2002).
8. R.W. Kelsall, Z. Ikonic, P. Murzyn, C.R. Pidgeon, P.J. Phillips, D. Carder, P. Harrison, S.A. Lynch, P. Townsend, D.J. Paul, S.L. Liew, D.J. Norris and A.G. Cullis, *Phys. Rev. B* **71**, 115326 (2006).
9. M. Califano, N.Q. Vinh, P.J. Phillips, Z. Ikonic, R.W. Kelsall, P. Harrison, C.R. Pidgeon, B.N. Murdin, D.J. Paul, P. Townsend, J. Zhang, I.M. Ross and A.G. Cullis, *Phys. Rev. B* **75**, 045338 (2007).
10. G. Dehlinger, L. Diehl, U. Gennser, H. Sigg, J. Faist, K. Ensslin, D. Grützmacher and E. Müller, *Science*, **290**, 2277 (2000).
11. L. Diehl, S. Mentese, E. Müller, D. Grützmacher , H. Sigg, U. Gennser, I. Sagnes, Y. Campidelli, O. Kermarrec, D. Bensahel and J. Faist., *Appl. Phys. Lett.*, **81**, 4700 (2002).
12. S.A. Lynch, R. Bates, D.J. Paul, D.J. Norris, A.G. Cullis, Z.Ikonic, R.W. Kelsall, P. Harrison, D.D. Arnone and C.R. Pidgeon, *Appl. Phys. Lett.*, **81**, 1543 (2002).
13. R. Bates, S.A. Lynch, D.J. Paul, Z. Ikonic, R.W. Kelsall, P. Harrison, D.J. Norris, S.L. Liew, A.G. Cullis, W. Tribe and D.D. Arnone, *Appl. Phys. Lett.*, **83**, 4092 (2003).
14. A. De Rossi, M. Carras and D.J. Paul, *IEEE J. Quantum Elec.*, **42**, 1233 (2006).
15. J. Faist, M. Beck, T. Aellen and E. Gini, *Appl. Phys. Lett.*, **78**, 147 (2001).
16. D.J. Paul, G. Matmon, P. Townsend, J. Zhang, M. Zhao and W.X. Ni, *IETE J. Research*, **53**, 285 (2007).
17. C. Rosenblad, H. von Känel, M. Kummar, A. Dormmann and E. Müller, *Appl. Phys. Lett.*, **76**, 427 (2000).
18. M. Enciso-Aguilar, F. Aniel, P. Crozat, R. Adde, H.-J. Herzog, T. Hackbarth, U. König and H. von Känel, *Elec. Lett.*, 39, 149 (2003).
19. S. Tsujino, H. Sigg, G. Mussler, D. Chrastina and H. von Känel, *Appl. Phys. Lett.*, **89**, 262119 (2006).
20. G. Isella, J. Osmond, M. Kummar, R. Kaufmann and H. von Känel, *Semicond. Sci. Technol.*, **22**, S26 (2007).
21. S.A. Lynch, S.S. Dhillon, R. Bates, D.J. Paul, D.D. Arnone, D.J. Robbins, Z. Ikonic, R.W. Kelsall, P. Harrison, D.J. Norris, A.G. Cullis, C.R. Pidgeon, P. Murzyn and A. Loudon, *Mat. Sci. Eng. B* **89**, 10 (2002).

22. S.A. Lynch, P. Townsend, G. Matmon, D.J. Paul, Z. Ikonic, R.W. Kelsall, P. Harrison, D.J. Norris, A.G. Cullis, and D.D. Arnone, *Appl. Phys. Lett.*, **87**, 101114 (2005).